

pubs.acs.org/JACS Article

# Interconversions between Uranium Mono-metallofullerenes: Mechanistic Implications and Role of Asymmetric Cages

Wenting Cai, Janet Alvarado, Alejandro Metta-Magaña, Ning Chen, and Luis Echegoyen\*



Cite This: https://dx.doi.org/10.1021/jacs.0c04888



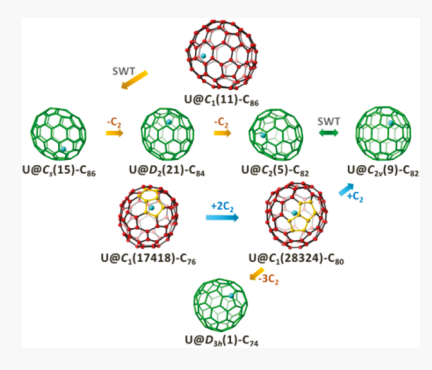
**ACCESS** 

Metrics & More

Article Recommendations

Supporting Information

**ABSTRACT:** The isolation and structural characterization of three new monometallic uranium metallofullerenes,  $U@D_2(21)$ - $C_{84}$ ,  $U@C_s(15)$ - $C_{86}$ , and  $U@C_1(11)$ - $C_{86}$ , allowed us to complete an interconversion map for all the characterized uranium monometallofullerenes. The topological analysis reveals that asymmetric fullerene cages, which may be formed by roll and wrap processes directly from graphene, are the starting points for a series of highly symmetric fullerene structures via top-down and bottom-up growth mechanisms. Moreover, some asymmetric intermediates, such as  $C_1(28324)$ - $C_{80}$ , can serve as precursors to form either larger cages in consecutive growing processes or smaller cages during cascade shrinking processes. This work provides evidence for both top-down and bottom-up processes happening simultaneously during the arcing processes. This study also sheds light on the prediction of possible cage structures for minor products produced in low yields in the soot.



## 1. INTRODUCTION

Fullerene cages, which are unstable in their empty form, can be stabilized by encapsulation of metal atoms and clusters. <sup>1,2</sup> To date, many fullerenes with variable isomeric cage structures and different sizes, which are not available in their pristine empty form, have been isolated and structurally characterized only as metallofullerenes. <sup>1–4</sup> The intercage transformations between these isolated endohedral metallofullerene (EMF) isomers, some of which are considered to play a key role in the growth path of fullerenes, are of special interest to understand the formation and growth mechanisms of fullerenes.

In contrast to some complicated routes, two facile processes, namely, Stone—Wales transformation (SWT)<sup>5</sup> and C<sub>2</sub>-insertion or extrusion, are supposed to be the more favored transformation pathways of fullerenes based on their relatively low energy barriers.<sup>6,7</sup> Multiple transformation pathways, based on these two processes, are established to connect fullerene cages, as shown in Figure 1. For example, some heptagon/pentalene-containing fullerene intermediates have been structurally characterized, such as  $Sc_2C_2@C_s(hept)-C_{88}$ ,  $LaSc_2N@C_s(hept)-C_{80}$ , and  $Sc_2S@C_s(10528)-C_{72}$ . Following relatively simple pathways, two mechanisms, i.e., the top-down and bottom-up mechanisms, have been proposed for fullerene formation.

In recent years, experimental support for the top-down mechanism has been reported. These reports proposed that smaller fullerenes can be formed via loss of carbon atoms from larger fullerene cages or even from graphene at high temperatures in an argon stream. The structural identification of Eu@C2(27)-C88, M2C2@C1(51383)-C84 (M = Gd and Y), and La2C2@C2(816)-C104 provided evidence for the top-down formation mechanism at the molecular level. 12–14

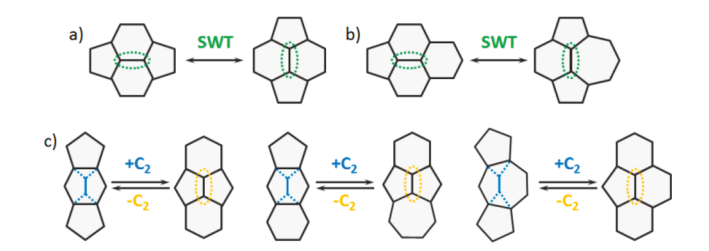


Figure 1. Multiple transformation pathways that interconvert fullerene cages. (a) Generalized SWT. (b) Formation of a heptagon through one SWT. (c) Formation of a pentalene or heptagon via  $C_2$  elimination/addition.  $C_2$  insertions are highlighted in blue, and  $C_2$  extrusions are highlighted in orange.

These cages are proposed to be intermediates for many existing, highly symmetric fullerenes with either IPR (isolated pentagon rule) or non-IPR structures. However, it is important to mention that  $C_2$  extrusion from an already closed fullerene requires more energy than  $C_2$  insertion under a rich carbon vapor atmosphere, whereby the formation of fullerenes might prefer to follow a bottom-up growth mechanism. <sup>6,15,16</sup> Consistently, the laser synthesis process of the  $U@C_{2n}$  and  $Ti@C_{2n}$  families demonstrate that the smallest stable fullerenes may act as precursors for the growth of fullerene cages. <sup>6,17</sup>

Received: May 4, 2020 Published: July 1, 2020



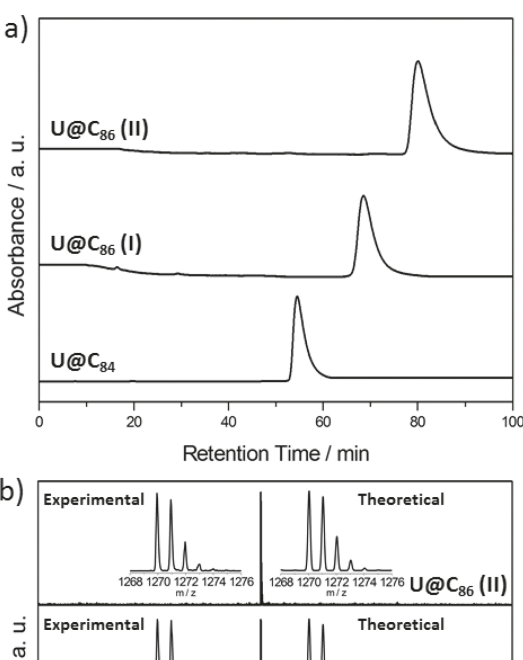
Nevertheless, due to the lack of in-situ experimental evidence, the formation and growth mechanisms of fullerenes are still open questions. Therefore, the carbon cage diversity of newly isolated EMFs will likely be helpful to establish more comprehensive mechanistic pathways for fullerene formation. Remarkably, our recent success in the isolation and characterizations of the non-IPR actinide EMFs demonstrated that "missing" fullerene cages could be stabilized in the form of actinide EMFs with a relative high product yield. Further topological studies show that the two non-IPR chiral cages,  $C_1(17418)$ - $C_{76}$  and  $C_1(28324)$ - $C_{80}$ , are enantiomerically connected by only two  $C_2$  insertions. We hypothesize and anticipate that some previously undiscovered fullerene cage structures could be stabilized by encapsulating actinide metals, which could provide new evidence to elucidate the formation and growth mechanisms of fullerenes.

Herein, the isolation and characterization of three novel uranium-containing metallofullerenes, namely,  $U@D_2(21)$ - $C_{84}$ ,  $U@C_s(15)$ - $C_{86}$ , and  $U@C_1(11)$ - $C_{86}$ , enabled us to assemble an interconverting chart including all of the characterized monometallic uranium EMFs. None of these three cages has been reported previously for lanthanide mono-EMFs. More importantly, the resulting interconverting chart suggests that the starting point in the rearrangement process via either top-down or bottom-up mechanistic steps seems to be the same asymmetric cage intermediate.

# 2. RESULTS AND DISCUSSION

2.1. Preparation, Purification, and Spectroscopic Characterizations of  $U@C_{2n}$  (2n = 84, 86). Soot containing  $U@C_{2n}$  (2n = 84, 86) was synthesized by a modified directcurrent arc-discharge method.<sup>22</sup> Graphite rods packed with  $U_3O_8$ /graphite powder (molar ratio of M/C = 1:24) were annealed and then vaporized in the arcing chamber under a 200 Torr helium atmosphere. The collected raw soot was then extracted using refluxing CS2 for 12 h. Multi-stage HPLC separation procedures were employed to isolate and purify U@ C<sub>84</sub> and U@C<sub>86</sub> (I, II) (see Figures S1-S3, Supporting Information). The purity of the isolated  $U@C_{84}$  and  $U@C_{86}$ (I, II) was confirmed by both HPLC and by MALDI-TOF mass spectroscopic analyses (Figure 2). The Vis-NIR absorption spectra of the three compounds are shown in Figure 3. All of them show obvious absorptions in the range from 400 to 1600 nm with very large optical bandgaps, reflecting relatively high thermodynamic stability. U@C<sub>84</sub> exhibits distinct absorptions at 807, 614, and 541 nm, while  $U@C_{86}(I)$  exhibits two absorptions at 869 and 649 nm. These absorption features are somewhat different from those of previously reported compounds containing C<sub>84</sub> and C<sub>86</sub> cages, which may indicate the presence of totally new  $C_{84}/C_{86}$  cage structures. The Vis-NIR absorption spectrum of  $U@C_{86}(II)$ displays two absorptions at 618 and 466 nm, which resemble those reported for Th@ $C_1(11)$ - $C_{86}$ .<sup>23</sup>

2.2. Crystallographic Identifications of  $U@D_2(21)$ - $C_{84}$ ,  $U@C_s(15)$ - $C_{86}$ , and  $U@C_1(11)$ - $C_{86}$ . The molecular structures of  $U@C_{84}$  and  $U@C_{86}$  (I, II) were determined using single-crystal X-ray diffraction (XRD). Co-crystals for the three compounds were obtained by layering a chloroform solution of



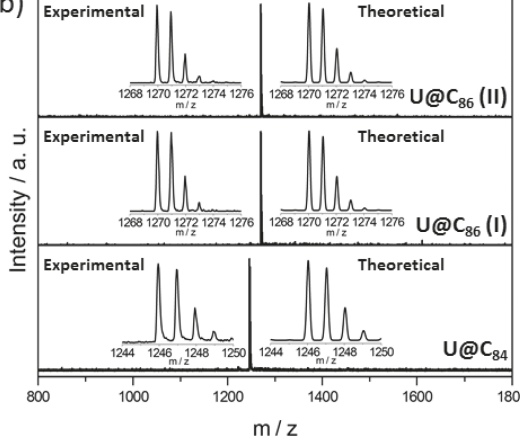


**Figure 2.** HPLC chromatograms of purified  $U@C_{84}$  and  $U@C_{86}$  (I, II) on a 5PBB column with toluene as the eluent at a flow rate of 1.5 mL·min<sup>-1</sup>. Insets show the positive mode MALDI-TOF mass spectra and expansions of the experimental and theoretical isotopic distributions of  $U@C_{84}$  and  $U@C_{86}$  (I, II).

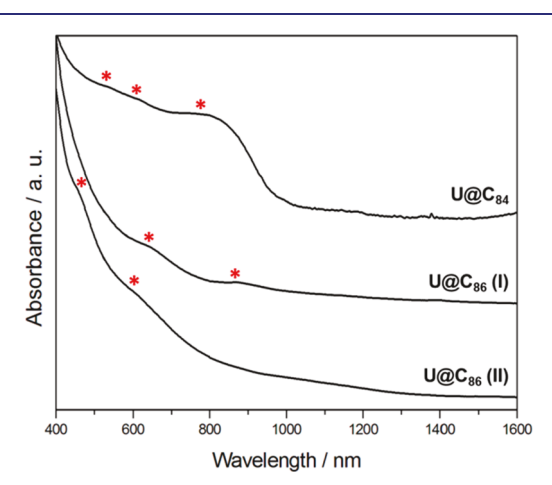
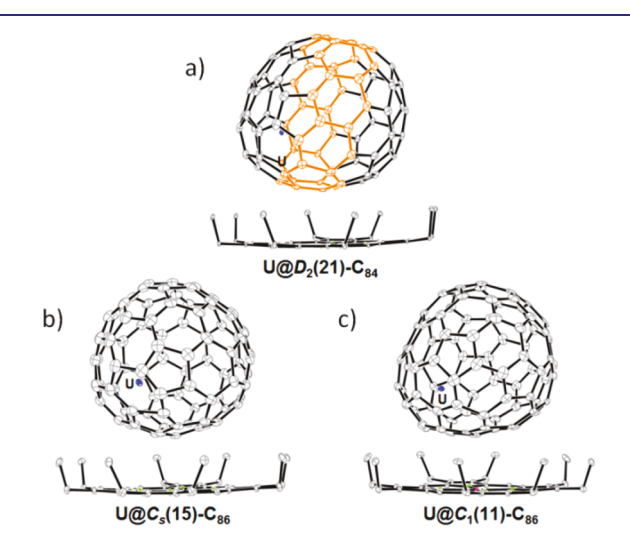


Figure 3. Vis-NIR absorption spectra of pure U@C $_{84}$  and U@C $_{86}$  (I, II) in CS $_2$ .

 $\mathrm{Ni^{II}}(\mathrm{OEP})$  (OEP = 2,3,7,8,12,13,17,18-octaethylporphyrin dianion) over a nearly saturated  $\mathrm{CS}_2$  solution of the purified endohedral metallofullerene. The crystal systems of all three compounds fall into the monoclinic space group  $C_2/m$ , where the asymmetric unit contains two halves of the carbon cage. Accordingly, the intact fullerene cage is generated by combining one half of the cage with the mirror image of the

other, both having an occupancy value of 0.50. Figure 4 shows the structures of the metallofullerenes and their relative



**Figure 4.** ORTEP drawings showing the relative orientations of the uranium endohedrals and the porphyrin ring for (a)  $U@D_2(21)-C_{84}$ :  $Ni^{II}(OEP)$ , (b)  $U@C_s(15)-C_{86}\cdot Ni^{II}(OEP)$ , and (c)  $U@C_1(11)-C_{86}\cdot Ni^{II}(OEP)$ . Thermal ellipsoids are shown at the 10% probability level, and the band of contiguous hexagons in  $D_2(21)-C_{84}$  is highlighted in orange. Only the major fullerene cage and the major uranium site are shown. Minor sites and solvent molecules are omitted for clarity.

orientations with respect to the co-crystallized  $Ni^{II}(OEP)$  molecules. The porphyrin ring faces a relatively flat region of each fullerene cage, with the shortest cage– $Ni^{II}(OEP)$  contacts ranging from 2.886 to 2.963 Å, due to  $\pi-\pi$  stacking interactions between each EMF molecule and the porphyrin ring.

Notably, the fullerene cages for U@C<sub>84</sub> and U@C<sub>86</sub> (I) are not the same IPR isomers found for the previously reported  $Sm@D_{3d}(19)\text{-}C_{84},^{24} Sm@C_2(13)\text{-}C_{84},^{24} Eu@D_{3d}(19)\text{-}C_{84},^{25} Eu@C_2(13)\text{-}C_{84},^{14} Eu@C_2(11)\text{-}C_{84},^{14} Yb@C_2(13)\text{-}C_{84},^{26} Eu@C_2(13)\text{-}C_{84},^{26} Eu@C_2(13)\text{-}C_{84},^{26} Eu@C_2(13)\text{-}C_{84},^{26} Eu@C_2(17)\text{-}C_{84},^{27} Lu_2@D_{2d}(23)\text{-}C_{84},^{28} Sc_2C_2@D_{2d}(23)\text{-}C_{84},^{29} Eu@C_1(7)\text{-}C_{86},^{14} Lu_2@C_s(8)\text{-}C_{86},^{27} Lu_2@C_2(9)\text{-}C_{86},^{28} Lu_2C_2@C_{2\nu}(9)\text{-}C_{86},^{27} Sc_2C_2@C_{2\nu}(9)\text{-}C_{86},^{19} Gd_3N@D_3(19)\text{-}C_{86},^{30} Tb_3N@D_3(19)\text{-}C_{86},^{31} and Lu_3N@D_3(19)\text{-}C_{86},^{32} Analysis of cage connectivity identified U@C_{84} as U@D_2(21)\text{-}C_{84} and U@C_{86} (I) as U@C_s(15)\text{-}C_{86} previously.}^{27} It is important to note that <math display="inline">D_2(21)\text{-}C_{84}$  is a totally new chiral cage, for which we observe the two enantiomers (cage 1 and cage 1A), see Figure S4. The crystallographic data indicate that U@C\_{86} (II) utilizes the  $C_1(11)\text{-}C_{86}$  cage, which is the same cage isomer found for Th@C\_1(11)-C\_{86} cage, which is the same cage isomer found for Th@C\_1(11)-C\_{86} cage, which is the same cage isomer found for Th@C\_1(11)-C\_{86} cage, which is the same cage isomer found for Th@C\_1(11)-C\_{86} cage, which is the same cage isomer found for Th@C\_1(11)-C\_{86} cage, which is the same cage isomer found for Th@C\_1(11)-C\_{86} cage, which is the same cage isomer found for Th@C\_1(11)-C\_{86} cage, which is the same cage isomer found for Th@C\_1(11)-C\_{86} cage, which is the same cage isomer found for Th@C\_1(11)-C\_{86} cage, which is the same cage isomer found for Th@C\_1(11)-C\_{86} cage, which is the same cage isomer found for Th@C\_1(11)-C\_{86} cage, which is the same cage isomer found for Th@C\_1(11)-C\_{86} cage, which is the same cage isomer found for Th@C\_1(11)-C\_{86} cage, which is the same cage isomer found for Th@C\_1(11)-C\_{86} cage, which is the same cage isomer found for Th@C\_1(11)-C\_{86} ca

The U ions in all three compounds exhibit some disorder, as shown in Figure 5. For  $U@D_2(21)$ - $C_{84}$ , seven U ion positions are observed, with fractional occupancies ranging from 0.3 to 0.01. Figure 5a shows all the identified metal sites within cage 1. Five of them are duplicated by the crystallographic mirror plane because they are not located at the symmetry plane. Interestingly, the arrangement of uranium atom sites in  $D_2(21)$ - $C_{84}$  is not distributed along the band of contiguous

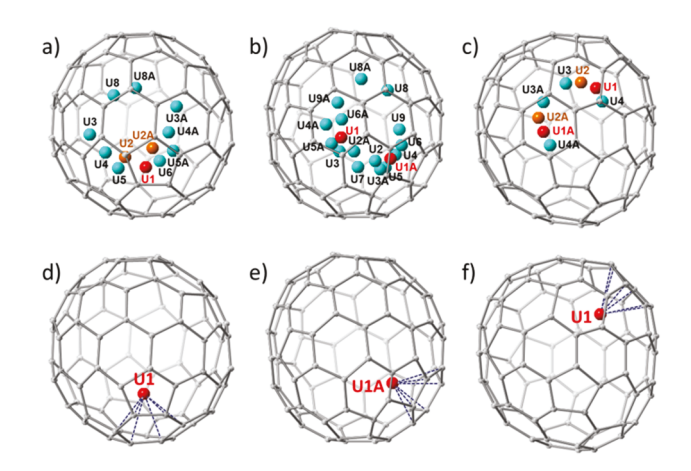


**Figure 5.** Perspective drawings showing the disordered uranium sites and the interaction of the major U site with the closest cage portion in (a, d)  $U@D_2(21)$ - $C_{84}$ , (b, e)  $U@C_s(15)$ - $C_{86}$ , and (c, f)  $U@C_1(11)$ - $C_{86}$ . The U atom labeled with "A" is generated by the crystallographic operation. The fractional occupancies for the major U sites (highlighted in red) in  $U@D_2(21)$ - $C_{84}$ ,  $U@C_s(15)$ - $C_{86}$ , and  $U@C_1(11)$ - $C_{86}$  are 0.30, 0.11, and 0.28, respectively. The U sites with relatively high occupancies (>0.10) are shown in orange, while the U sites with low occupancies (0.01–0.08) are shown in blue.

hexagons, which is different from what was reported previously for  $U(@C_{2\nu}(9)-C_{82\nu}^{33} \text{ Sm}(@C_2(40)-C_{90\nu}^{34} \text{ Sm}(@C_2(42)-C_{90\nu}^{34} \text{ Sm}(@C_2(42)-C_{90\nu}^{34} \text{ Sm}(@C_2(42)-C_{90\nu}^{34} \text{ The major metal site U1 (0.3 occupancy) is residing on the crystallographic mirror plane. A closer look reveals that U1 is situated under the center of a hexagon with the closest U-cage contacts in the range of 2.202 (14)–2.36 (3) Å (as shown in Figure 5d and Figure S5).$ 

Similarly, there are nine U ion positions with fractional occupancies ranging from 0.11 to 0.03 for U@C<sub>s</sub>(15)-C<sub>86</sub>. Only U7 (0.03 occupancy) resides at the symmetry plane; eight additional metal sites are generated via the crystallographic mirror plane (as shown in Figure 5b). The primary U atom U1 (0.11 occupancy) is situated over a [6,6]-bond junction with very short U-cage distances of 1.87 (4) and 2.02 (3) Å, whereas U1A (the mirror-related site of U1) is located over the center of a hexagon with an average closest U-cage contact of 2.206 (6) Å (Figure 5e and Figure S6). Even though both locations are identically occupied from the crystallographic perspective, the U1A-cage distances are similar to the typical U-cage contacts reported in our previous crystallographic results, whereas the U1-cage distances are too short to correspond to real U-cage distances. Accordingly, the U1A occupancy is assigned as the most stable structure for the cage orientation shown in Figure 5e.

For U@ $C_1(11)$ - $C_{86}$ , only four U ion positions were observed, with fractional occupancies of 0.28, 0.17, 0.03, and 0.02. Another four positions, namely, U1A, U2A, U3A, and U4A, were generated via the crystallographic operation (as shown in Figure 5c). As compared to the multiple positions for U in the  $C_s(15)$ - $C_{86}$  cage, the movement of the U atom in the  $C_1(11)$ - $C_{86}$  cage is relatively hindered. Similar positional distributions have also been reported previously for the crystallographic structures of U@ $C_1(28324)$ - $C_{80}$ , and Th@ $C_1(11)$ - $C_{86}$ , thus indicating that the cage symmetry may play an important role on the movement of the metal atom inside the fullerene cage. Note that the  $C_1(11)$ - $C_{86}$  cage is chiral, so the two cage orientations

(cage 1 and cage 1A) are actually enantiomeric species (as shown in Figure S7). Figure 5f and Figure S8 show the major site of the U atom in cage 1. The primary U atom U1 (0.28 occupancy) is situated over the center of a hexagon with the closest U-cage contacts in the range of 2.31 (2)-2.399 (2) Å, very similar to the major Th site in Th@ $C_1$ (11)- $C_{86}$ .<sup>23</sup>

**2.3. Electrochemical Properties for U@** $D_2$ (21)- $C_{84}$ , U@  $C_s$ (15)- $C_{86}$ , and U@ $C_1$ (11)- $C_{86}$ . The electrochemical properties of U@ $D_2$ (21)- $C_{84}$ , U@ $C_s$ (15)- $C_{86}$ , and U@ $C_1$ (11)- $C_{86}$  were investigated by means of cyclic voltammetry (CV) using a glassy carbon working electrode in *ortho*-dichlorobenzene (*o*-DCB) containing tetra(n-butyl)ammonium hexafluorophosphate (TBAPF<sub>6</sub>) as supporting electrolyte (see Figure 6). All of the redox processes of U@ $D_2$ (21)- $C_{84}$ , U@ $C_s$ (15)-

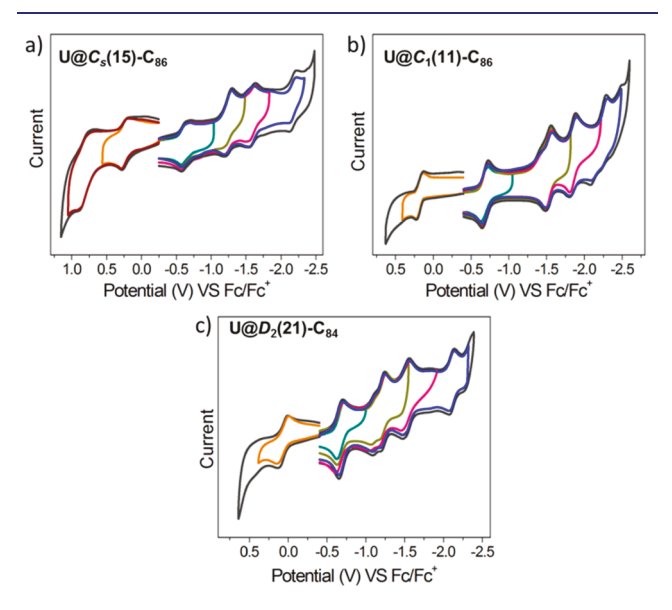


**Figure 6.** Cyclic voltammograms of (a)  $U@C_s(15)$ - $C_{86}$ , (b)  $U@C_1(11)$ - $C_{86}$ , and (c)  $U@D_2(21)$ - $C_{84}$  in o-dichlorobenzene (0.05 M  $(n\text{-Bu})_4\text{NPF}_6$ ; scan rate 100 mV/s for CV).

 $C_{86}$ , and  $U@C_1(11)$ - $C_{86}$  are electrochemically reversible. Both  $U@D_2(21)$ - $C_{84}$  and  $U@C_1(11)$ - $C_{86}$  display four reductive steps and one oxidative step, whereas four reductive steps and two oxidative steps were observed for  $U@C_s(15)$ - $C_{86}$ . The observed redox potentials of these three compounds are summarized in Table 1. As expected, the influence of the cage structures on the electrochemical potentials is obvious. The first reduction potentials for  $U@D_2(21)$ - $C_{84}$ ,  $U@C_s(15)$ - $C_{86}$ , and  $U@C_1(11)$ - $C_{86}$  are almost identical, indicating that the lowest unoccupied molecular orbital (LUMO) is unaffected by the cage symmetry. However, their first oxidation potentials are very different. The first oxidation potential for  $U@C_1(11)$ - $C_{86}$  (0.18 V) is 60 mV lower than that for  $U@C_s(15)$ - $C_{86}$  (0.24 V). The first oxidation potential for  $U@D_2(21)$ - $C_{84}$  is even

more cathodically shifted to 0.07 V, giving rise to a relatively smaller electrochemical gap of 0.75 V. This result also correlates well with the optical band gap calculated from the UV-Vis-NIR absorption. It is worth noting that the first reduction potential of  $U@C_1(11)$ - $C_{86}$  is at -0.69 V, which is far more positive than that for Th@ $C_1(11)$ - $C_{86}$  (-1.17 V),<sup>23</sup> resulting in a relatively smaller electrochemical gap of 0.87 V, compared to 1.38 V for Th@ $C_1(11)$ - $C_{86}$ . A similar phenomenon was observed for U@C1(28324)-C80 and Th@  $C_1(28324)$ - $C_{80}$ . Our previous frontier molecular orbital analyses showed that the energies of the Th empty orbitals are higher than those of the cage orbitals, whereas the U 5f orbitals are quite low in energy. As a result, the LUMO is localized on the carbon cage for Th@ $C_1(28324)$ - $C_{80}$  but on the metal for  $U@C_1(28324)$ - $C_{80}$ . The completely different location of the LUMOs for Th mono-EMFs and U mono-EMFs significantly affects where their reduction processes take place and eventually generates a large difference in their electrochemical gaps.

2.4. Interconversion Diagram for Uranium Monometallofullerenes. We recently reported that a series of monometallic uranium EMFs with cages ranging from C<sub>74</sub> to C<sub>104</sub> were obtained by arcing graphite rods filled with uranium oxide and graphite powder by a modified direct-current arcdischarge method. In this family, the molecular structures of the most abundant species, that is,  $U@D_{3h}(1)-C_{74}$ ,  $^{33}$   $U@C_1(17418)-C_{76}$ ,  $^{21}$   $U@C_1(28324)-C_{80}$ ,  $^{21}$   $U@C_2(5)-C_{82}$ ,  $^{33}$   $U@C_1(28324)-C_{80}$ ,  $^{21}$  $C_{2\nu}(9)$ - $C_{82}$ , <sup>33</sup> U@ $D_2(21)$ - $C_{84}$ (this study), U@ $C_1(11)$ - $C_{86}$  (this study), and  $U @ C_s(15) - C_{86}$  (this study), have been characterized by single-crystal XRD. It is worth noting that three of them possess  $C_1$ -symmetric fullerene cages:  $C_1(17418)$ - $C_{76}$ ,  $C_1(28324)$ - $C_{80}$ , and  $C_1(11)$ - $C_{86}$ . Interestingly, our topological analysis reveals that  $C_1(11)$ - $C_{86}$  and  $C_1(17418)$ - $C_{76}$  are obtainable via spontaneous rolling and wrapping directly from flat graphene sheets (Figure 7). Likewise, another lowsymmetry fullerene cage,  $C_2(27)$ - $C_{88}$ , was also supposed to be obtained by the rolling and wrapping of a graphene fragment. 14 Although the specific transformation routes are still not fully understood, previous transmission electron microscopy studies provided direct evidence for fullerene formation directly from graphene sheets. 11 Besides, the  $C_1(28324)$ - $C_{80}$  cage is enantiomerically correlated to the  $C_1(17418)$ - $C_{76}$  cage. Enantiomer e1 (e2) of  $C_1(17418)$ - $C_{76}$  and enantiomer e2 (e1) of  $C_1(28324)$ - $C_{80}$  are topologically connected by only two C<sub>2</sub> insertions with no rearrangements needed. Unexpectedly, based on the cage structures of  $U@C_1(17418)-C_{76}$ , U@ $C_1(28324)$ - $C_{80}$ , and  $U@C_1(11)$ - $C_{86}$ , we are now able to complete an interconversion map for all of characterized monometallic uranium EMFs. More importantly, some new cages are also involved in these processes according to the topological correlation. We propose that the presence of these cages may play an important role in predicting the possible cage structures for minor products with low yield.

Table 1. Redox Potentials (V vs Fc/Fc<sup>+</sup>)<sup>a</sup> and Electrochemical Bandgaps of U@ $D_2(21)$ -C<sub>84</sub>, U@ $C_s(15)$ -C<sub>86</sub>, and U@ $C_1(11)$ -C<sub>86</sub>

species	$^{\mathrm{ox}}E_{2}$	$^{\text{ox}}E_1$	$^{ m red}E_1$	$^{ m red}E_2$	$^{ m red}E_3$	$^{ m red}E_4$	$\Delta E_{ m gap}$
$U@D_2(21)-C_{84}$	_	0.07	-0.68	-1.22	-1.55	-2.12	0.75
$U@C_s(15)-C_{86}$	0.82	0.24	-0.60	-1.28	-1.57	-2.19	0.84
$U@C_1(11)-C_{86}$	_	0.18	-0.69	-1.54	-1.86	-2.26	0.87

<sup>&</sup>lt;sup>a</sup>Half-cell potentials (reversible redox process).

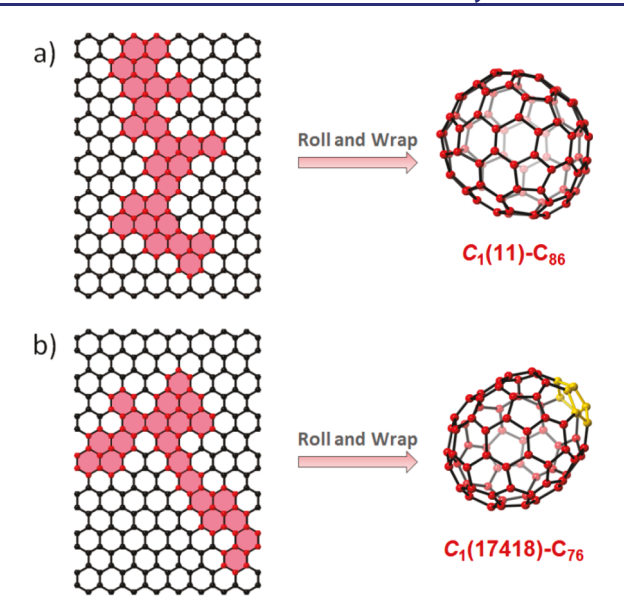


**Figure 7.** Hypothesized formation of (a)  $C_1(11)$ - $C_{86}$  and (b)  $C_1(17418)$ - $C_{76}$  through spontaneous self-assembly of flat graphene sheets.

Figure 8 depicts the interconversion map, and the detailed pathways are illustrated in the Supporting Information (Figures S9–S17). On the one hand, three [5,5]- $C_2$  extrusions with a subsequent SWT on  $C_1(28324)$ - $C_{80}$  produce  $D_{3h}(1)$ - $C_{74}$  directly. On the other hand, the transformation from  $C_1(11)$ - $C_{86}$  to  $C_s(15)$ - $C_{86}$  is straightforward via a single SWT. Afterward, elimination of a  $C_2$  unit from a pentalene unit generated by one SWT on  $C_s(15)$ - $C_{86}$  affords  $C_s(10)$ - $C_{84}$ . In further steps,  $D_2(21)$ - $C_{84}$  can be obtained via one SWT from  $C_s(10)$ - $C_{84}$ , while  $C_{2\nu}(9)$ - $C_{82}$  is formed from  $C_s(10)$ - $C_{84}$  through a SWT and a subsequent [5,5]- $C_2$  extrusion. The isomerizations between three  $C_{82}$  cages, namely,  $C_{2\nu}(9)$ - $C_{82}$ ,  $C_s(6)$ - $C_{82}$ , and  $C_2(5)$ - $C_{82}$ , are related by a single SWT each.

In addition to the top-down process, we noticed that  $C_1(28324)$ - $C_{80}$  can also be a potential precursor for  $C_{2\nu}(9)$ - $C_{82}$ ,  $C_s(6)$ - $C_{82}$ , and  $C_2(5)$ - $C_{82}$  via a bottom-up mechanism. First,  $C_1(28324)$ - $C_{80}$  undergoes a SWT to form  $C_1(\text{hept})$ - $C_{80}$ . Interestingly, a simple  $C_2$  insertion at the heptagon results in the generation of  $C_s(6)$ - $C_{82}$ . Subsequently,  $C_{2\nu}(9)$ - $C_{82}$  and  $C_2(5)$ - $C_{82}$  are obtainable from  $C_s(6)$ - $C_{82}$  via a single SWT each

Clearly, our topological analysis reveals that fullerene cages with low symmetry, which may be formed directly from graphene, play important roles as starting points for metallofullerene transformations via top-down and bottom-up processes. This observation is also corroborated by previous studies of  $C_2(816)$ - $C_{104}$  (obtained in the form of  $La_2C_2$ @  $C_2(816)-C_{104}$ ),  $C_2(27)-C_{88}$  (obtained in the form of Eu@  $C_2(27)$ - $C_{88}$ ), and  $C_1(51383)$ - $C_{84}$  (obtained in the form of  $Gd_2C_2@C_1(51383)-C_{84}$ ). These compounds are considered to be the key structures in the transformation map for most of the characterized metallofullerenes. 12-14 Likewise, Sc<sub>2</sub>S@  $C_2(7892)$ - $C_{70}$  was found to be the potential precursor of  $Sc_2S@C_s(10528)-C_{72}$  via a bottom-up growth. 10,18 More interestingly, in contrast to the above-mentioned lowsymmetry cages,  $C_1(28324)$ - $C_{80}$  can evolve into either smaller highly symmetric cages via cascade shrinking processes or larger highly symmetric cages via consecutive growing processes. To the best of our knowledge, this analysis

represents the first example that shows that the starting point for a top-down or bottom-up mechanistic transformation can arise from the same asymmetric intermediates. Based on these observations, we anticipate that the  $C_1(11)$ - $C_{86}$  cage may serve as a key link for the formation of some larger cages (such as  $C_{90}$  isomers) via the insertion of  $C_2$  units in a bottom-up process.

It should also be noticed that all of the compounds included in this transformation matrix belong to the family of  $U@C_{2n}$  (2n = 74-104), which were produced under the same arcing conditions. Therefore, all the transformation routes ( $C_2$  insertion and  $C_2$  extrusion) mentioned in Figure 8 likely occur simultaneously. Kroto and colleagues proposed that the insertion of  $C_2$  units to small carbon nanoclusters and fullerene cages is less energetically demanding than the extrusion of them when there is enough carbon vapor concentration in the surrounding atmosphere. In addition, it has also been found that smaller fullerene cages can be formed via  $C_2$  extrusions from larger fullerene cages or even from graphene under a low carbon vapor atmosphere. In this regard, we conclude that the top-down and bottom-up processes may happen simultaneously in the arcing process.

It is worth mentioning that a series of minor isomers of U@  $C_{2n}$  were detected along with the major products. The cage structures of these minor isomers have not been characterized so far due to the extremely low yields. In this regard, we speculate that  $C_1(\text{hept})$ - $C_{80}$ ,  $C_s(6)$ - $C_{82}$ , and  $C_s(10)$ - $C_{84}$  are most likely candidates based on their topological correlations with the other existing cage isomers shown in Figure 8. We acknowledge that our proposed scheme is not the only possible transformation matrix for monometallic uranium EMFs. The minor products might follow other transformation routes as well. New asymmetric cages are likely to be found as starting points for different transformation matrices in the future.

#### 3. CONCLUSIONS

In summary, three new monometallic uranium metallofullerenes,  $U@D_2(21)-C_{84}$ ,  $U@C_s(15)-C_{86}$ , and  $U@C_1(11)-C_{86}$ C<sub>86</sub>, have been successfully synthesized and fully characterized by mass spectrometry, single-crystal X-ray diffractometry, UVvis-NIR, and cyclic voltammetry. Along with the characterization of these fullerene cages, an interconversion map including all of the characterized uranium mono-metallofullerenes is presented. The topological analysis reveals that the same asymmetric fullerene cages can lead to the formation of many highly symmetric fullerene structures via either top-down or bottom-up processes. This work provides evidence to demonstrate that both top-down and bottom-up processes may happen simultaneously during the arcing process. The topological interconversion diagram provides the basis for future in-depth theoretical calculations of the possible intermediates and energy barriers.

# 4. EXPERIMENTAL SECTION

**4.1. Synthesis and Isolation of U@C**<sub>2n</sub> (2n = 84, 86). The carbon soots containing U@C<sub>2n</sub> (2n = 84, 86) were synthesized by the direct-current arc-discharge method. The graphite rods, packed with U<sub>3</sub>O<sub>8</sub>/graphite powder in a molar ratio of 1:24, were vaporized in the arcing chamber under 200 Torr He. The resulting soot was extracted using refluxing CS<sub>2</sub> under an argon atmosphere for 12 h. The separation and purification of U@C<sub>2n</sub> (2n = 84, 86) were achieved by multi-stage high-performance liquid chromatography (HPLC) procedures. Multiple HPLC columns, including a Bucky-

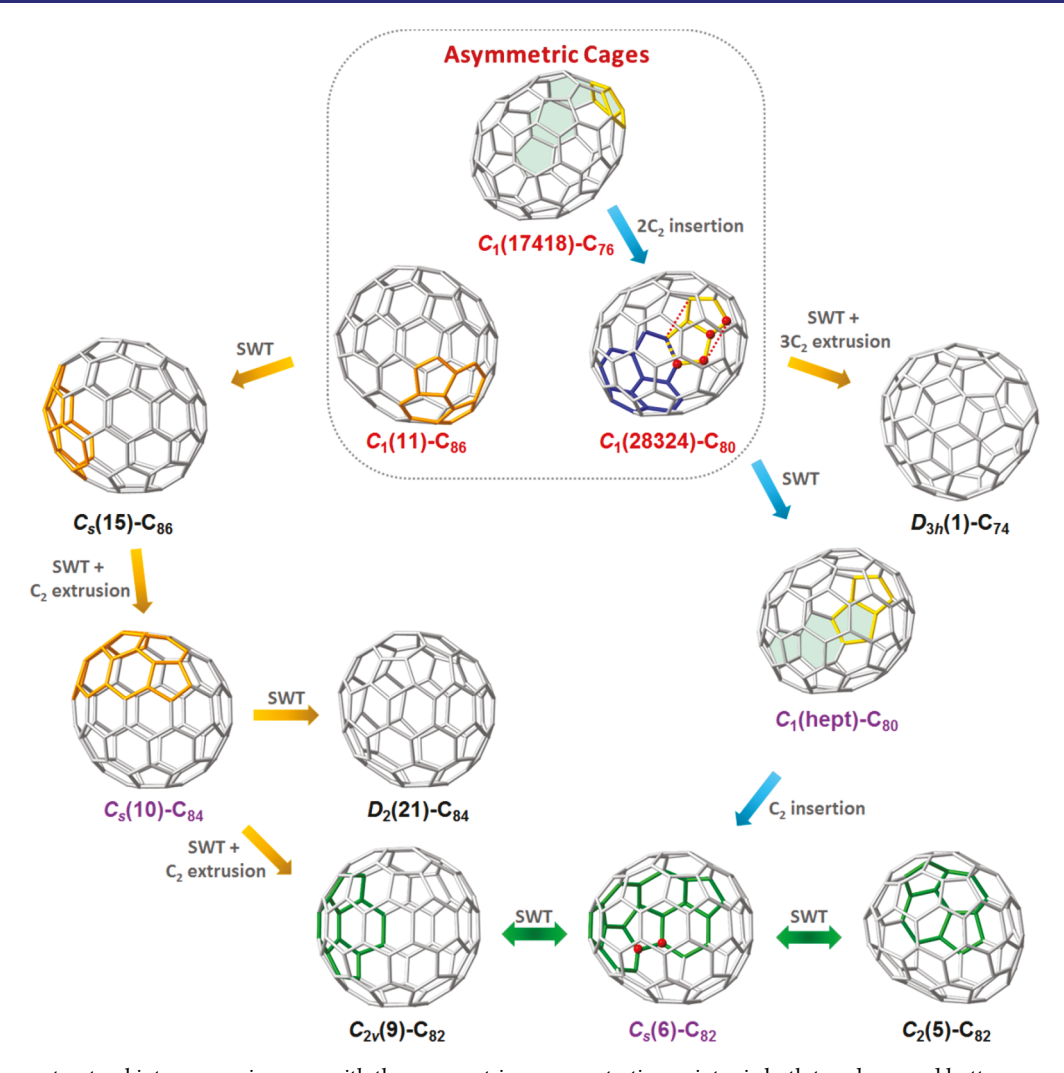


**Figure 8.** Fullerene structural interconversion map with the asymmetric cages as starting points via both top-down and bottom-up processes. All the presently characterized uranium mono-metallofullerenes are included in this diagram, while potential minor products are highlighted in purple. The top-down processes are indicated by orange arrows, while the bottom-up processes are indicated by blue arrows. The fused pentagons in the cage framework are highlighted in yellow. The atoms in orange, blue, and green indicate the starting points in the top-down process, the bottom-up process, and the SWT interconversion, respectively. The detailed pathways are illustrated in the Supporting Information (Figures S8–S16).

prep-M column ( $10 \times 250$  mm), a Buckyprep-D column ( $10 \times 250$  mm), and a Buckyprep column ( $10 \times 250$  mm) (all Cosmosil, Nacalai Tesque, Kyoto, Japan), were utilized in this procedure. Further details are described in the Supporting Information.

- **4.2. Spectroscopic Studies.** Laser desorption/ionization time-of-flight (LDI-TOF) mass spectrometry was measured on a Bruker LRF MALDI spectrometer. Ultraviolet—visible—near-infrared (UV-Vis-NIR) spectra of the purified U@ $C_{2n}$  (2n=84,86) in CS<sub>2</sub> solution were measured with a Cary 5000 UV-Vis-NIR spectrophotometer.
- **4.3. Electrochemical Studies.** Cyclic voltammetry (CV) results were measured in *o*-dichlorobenzene with 0.05 M (*n*-Bu)<sub>4</sub>NPF<sub>6</sub> as the supporting electrolyte using a CH Instruments potentiostat. A conventional three-electrode cell consisting of a platinum counterelectrode, a glassy carbon working electrode, and a silver reference electrode was used for all measurements. All potentials were reported relative to the Fc/Fc<sup>+</sup> couple.
- **4.4. Single-Crystal X-ray Diffraction.** Crystalline blocks of U@  $C_{2n}$  (2n = 84, 86) were obtained by layering a chloroform solution of Ni<sup>II</sup>(OEP) over a nearly saturated solution of the respective endohedral in CS<sub>2</sub> in a glass tube. Over a 20-day period, the two solutions diffused into each other, and black crystals formed. XRD measurements were performed at 150 K on a Bruker APEX-II CCD diffractometer. The multi-scan method was used for absorption corrections. The structures were solved by a direct method and

refined with SHELXL-2018.<sup>36</sup> Hydrogen atoms were inserted at calculated positions and constrained with isotropic thermal parameters.

Crystal data for U@ $D_2(21)$ -C<sub>84</sub>·Ni<sup>II</sup>(OEP)·CHCl<sub>3</sub>·2CS<sub>2</sub>: C<sub>123</sub>H<sub>45</sub>Cl<sub>3</sub>N<sub>4</sub>NiS<sub>4</sub>U,  $M_{\rm w}=2109.94$ , monoclinic, space group  $C_2/m$ , a=25.3499(10) Å, b=15.6119(6) Å, c=19.4382(8) Å,  $\beta=93.644(1)^\circ$ , V=7677.3(5) Å<sup>3</sup>, Z=4, T=150 K,  $\rho_{\rm calcd}=1.826$  Mg m<sup>-3</sup>,  $\mu({\rm MoK}\alpha)=2.634$  mm<sup>-1</sup>, 46 113 reflections measured, 9928 unique ( $R_{\rm int}=0.0556$  used in all calculations). The final w $R_2$  was 0.3224 (all data) and  $R_1$  (6030 with  $I>2\sigma(I)$ ) was 0.0983. CCDC 1835948 contains the crystallographic data; CIF files are available as Supporting Information.

Crystal data for U@ $C_s(15)$ -C $_{86}$ -Ni<sup>II</sup>(OEP)·CHCl $_3$ ·2CS $_2$ : C $_{125}$ H $_{45}$ Cl $_3$ N $_4$ NiS $_4$ U,  $M_w$  = 2133.96, monoclinic, space group  $C_2/m$ , a = 25.327(4) Å, b = 15.319(3) Å, c = 19.913(3) Å,  $\beta$  = 93.943(3)°, V = 7708(2) Å $_3$ , Z = 4, T = 150 K,  $\rho_{\rm calcd}$  = 1.839 Mg m $_3$ ,  $\mu$ (MoK $\alpha$ ) = 2.625 mm $_3$ , 43 798 reflections measured, 9959 unique ( $R_{\rm int}$  = 0.1003 used in all calculations). The final w $R_2$  was 0.3380 (all data) and  $R_1$  (3499 with I > 2 $\sigma$ (I) was 0.1380. CCDC 1996261 contains the crystallographic data; CIF files are available as Supporting Information.

Crystal data for  $U@C_1(11) - C_{86} \cdot Ni^{11}(OEP) \cdot 2CS_2$ :  $C_{124}H_{44}N_4NiS_4U$ ,  $M_w = 2014.59$ , monoclinic, space group  $C_2/m$ , a = 25.446(9) Å, b = 15.236(5) Å, c = 19.948(7) Å,  $\beta = 94.021(4)^\circ$ ,  $V = 10.021(4)^\circ$ , V = 10

7715(5) ų, Z=4, T=150 K,  $\rho_{\rm calcd}=1.735$  Mg m³,  $\mu({\rm MoK}\alpha)=2.516$  mm¹, 20 240 reflections measured, 9414 unique ( $R_{\rm int}=0.0690$  used in all calculations). The final w $R_2$  was 0.3372 (all data) and  $R_1$  (4753 with  $I>2\sigma(I)$ ) was 0.1039. CCDC 1996257 contains the crystallographic data; CIF files are available as Supporting Information.

## ASSOCIATED CONTENT

## **Supporting Information**

The Supporting Information is available free of charge at https://pubs.acs.org/doi/10.1021/jacs.0c04888.

HPLC profiles for the separation of  $U@D_2(21)$ - $C_{84}$ ,  $U@C_s(15)$ - $C_{86}$ , and  $U@C_1(11)$ - $C_{86}$ ; crystallographic solutions and additional X-ray results of  $U@D_2(21)$ - $C_{84}$ ,  $U@C_s(15)$ - $C_{86}$ , and  $U@C_1(11)$ - $C_{86}$ ; and detailed transformation pathways between monometallic uranium EMFs, including Figures S1–S17 (PDF)

X-ray crystallographic data for U@ $C_1(11)$ - $C_{86}$  (CIF) X-ray crystallographic data for U@ $C_s(15)$ - $C_{86}$  (CIF)

X-ray crystallographic data for U@D<sub>2</sub>(21)-C<sub>84</sub> (CIF)

# AUTHOR INFORMATION

#### **Corresponding Author**

Luis Echegoyen — Department of Chemistry, University of Texas at El Paso, El Paso, Texas 79968, United States; orcid.org/0000-0003-1107-9423; Email: echegoyen@utep.edu

#### **Authors**

Wenting Cai − Department of Chemistry, University of Texas at El Paso, El Paso, Texas 79968, United States; orcid.org/0000-0003-3653-1711

Janet Alvarado – Department of Chemistry, University of Texas at El Paso, El Paso, Texas 79968, United States

Alejandro Metta-Magaña — Department of Chemistry, University of Texas at El Paso, El Paso, Texas 79968, United States; orcid.org/0000-0001-9993-8485

Ning Chen – College of Chemistry, Chemical Engineering and Materials Science, Soochow University, Suzhou, Jiangsu 215123, P. R. China; orcid.org/0000-0002-9405-6229

Complete contact information is available at: https://pubs.acs.org/10.1021/jacs.0c04888

#### Notes

The authors declare no competing financial interest.

## ACKNOWLEDGMENTS

L.E. thanks the Robert A. Welch Foundation for an endowed chair (Grant No. AH-0033) and the U.S. NSF (Grant No. CHE-1801317) for generous financial support. Crystallographic data was made possible by support from the NSF-MRI program (CHE-1827875). N. C. thanks the National Science Foundation China (NSFC 91961109, 51302178) for financial support.

## REFERENCES

- (1) Popov, A. A.; Yang, S.; Dunsch, L. Endohedral Fullerenes. *Chem. Rev.* **2013**, *113*, 5989–6113.
- (2) Lu, X.; Echegoyen, L.; Balch, A. L.; Nagase, S.; Akasaka, T. Endohedral Metallofullerenes: Basics and Applications; CRC Press,
- (3) Yang, S.; Wei, T.; Jin, F. When metal clusters meet carbon cages: endohedral clusterfullerenes. *Chem. Soc. Rev.* **2017**, *46*, 5005–5058.

- (4) Lu, X.; Feng, L.; Akasaka, T.; Nagase, S. Current status and future developments of endohedral metallofullerenes. *Chem. Soc. Rev.* **2012**. *41*. 7723–7760.
- (5) Stone, A. J.; Wales, D. J. Theoretical studies of icosahedral  $C_{60}$  and some related species. *Chem. Phys. Lett.* **1986**, 128, 501–503.
- (6) Mulet-Gas, M.; Abella, L.; Dunk, P. W.; Rodríguez-Fortea, A.; Kroto, H. W.; Poblet, J. M. Small endohedral metallofullerenes: exploration of the structure and growth mechanism in the  $\text{Ti}@\text{C}_{2n}$  (2n = 26–50) family. *Chem. Sci.* **2015**, *6*, 675–686.
- (7) Cross, R. J.; Saunders, M. Transmutation of fullerenes. *J. Am. Chem. Soc.* **2005**, 127, 3044–3047.
- (8) Chen, C.-H.; Abella, L.; Cerón, M. R.; Guerrero-Ayala, M. A.; Rodríguez-Fortea, A.; Olmstead, M. M.; Powers, X. B.; Balch, A. L.; Poblet, J. M.; Echegoyen, L. Zigzag  $Sc_2C_2$  Carbide Cluster inside a [88]Fullerene Cage with One Heptagon,  $Sc_2C_2@C_s(hept)-C_{88}$ : A Kinetically Trapped Fullerene Formed by  $C_2$  Insertion? *J. Am. Chem. Soc.* **2016**, *138*, 13030–13037.
- (9) Zhang, Y.; Ghiassi, K. B.; Deng, Q.; Samoylova, N. A.; Olmstead, M. M.; Balch, A. L.; Popov, A. A. Synthesis and Structure of LaSc<sub>2</sub>N@ $C_s(hept)$ - $C_{80}$  with One Heptagon and Thirteen Pentagons. *Angew. Chem., Int. Ed.* **2015**, *54*, 495–499.
- (10) Chen, N.; Beavers, C. M.; Mulet-Gas, M.; Rodriguez-Fortea, A.; Munoz, E. J.; Li, Y. Y.; Olmstead, M. M.; Balch, A. L.; Poblet, J. M.; Echegoyen, L.  $Sc_2S@C_s(10528)-C_{72}$ : A Dimetallic Sulfide Endohedral Fullerene with a Non Isolated Pentagon Rule Cage. *J. Am. Chem. Soc.* **2012**, *134*, 7851–7860.
- (11) Chuvilin, A.; Kaiser, U.; Bichoutskaia, E.; Besley, N. A.; Khlobystov, A. N. Direct transformation of graphene to fullerene. *Nat. Chem.* **2010**, 2, 450–453.
- (12) Zhang, J.; Bowles, F. L.; Bearden, D. W.; Ray, W. K.; Fuhrer, T.; Ye, Y.; Dixon, C.; Harich, K.; Helm, R. F.; Olmstead, M. M.; Balch, A. L.; Dorn, H. C. A missing link in the transformation from asymmetric to symmetric metallofullerene cages implies a top-down fullerene formation mechanism. *Nat. Chem.* **2013**, *5*, 880.
- (13) Cai, W.; Li, F.-F.; Bao, L.; Xie, Y.; Lu, X. Isolation and Crystallographic Characterization of  $La_2C_2@C_s(574)-C_{102}$  and  $La_2C_2@C_2(816)-C_{104}$ : Evidence for the Top-Down Formation Mechanism of Fullerenes. *J. Am. Chem. Soc.* **2016**, 138, 6670–6675.
- (14) Bao, L.; Yu, P.; Pan, C.; Shen, W.; Lu, X. Crystallographic identification of Eu@ $C_{2n}$  (2n = 88, 86 and 84): completing a transformation map for existing metallofullerenes. *Chem. Sci.* **2019**, *10*, 2153.
- (15) Dunk, P. W.; Kaiser, N. K.; Hendrickson, C. L.; Quinn, J. P.; Ewels, C. P.; Nakanishi, Y.; Sasaki, T.; Shinohara, H.; Marshall, A. G.; Kroto, H. W. Closed network growth of fullerenes. *Nat. Commun.* **2012**, *3*, 855.
- (16) Dunk, P. W.; Mulet-Gas, M.; Nakanishi, Y.; Kaiser, N. K.; Rodríguez-Fortea, A.; Shinohara, H.; Poblet, J. M.; Marshall, A. G.; Kroto, H. W. Bottom-up formation of endohedral mono-metallofullerenes is directed by charge transfer. *Nat. Commun.* **2014**, *5*, 5844. (17) Dunk, P. W.; Kaiser, N. K.; Mulet-Gas, M.; Rodríguez-Fortea,
- (17) Dunk, P. W.; Kaiser, N. K.; Mulet-Gas, M.; Rodriguez-Fortea, A.; Poblet, J. M.; Shinohara, H.; Hendrickson, C. L.; Marshall, A. G.; Kroto, H. W. The Smallest Stable Fullerene, M@C<sub>28</sub> (M = Ti, Zr, U): Stabilization and Growth from Carbon Vapor. *J. Am. Chem. Soc.* **2012**, 134, 9380–9389.
- (18) Chen, N.; Mulet-Gas, M.; Li, Y. Y.; Stene, R. E.; Atherton, C. W.; Rodriguez-Fortea, A.; Poblet, J. M.; Echegoyen, L.  $Sc_2S@C_2(7892)-C_{70}$ : a metallic sulfide cluster inside a non-IPR  $C_{70}$  cage. Chem. Sci. **2013**, 4, 180–186.
- (19) Chen, C.-H.; Ghiassi, K. B.; Cerón, M. R.; Guerrero-Ayala, M. A.; Echegoyen, L.; Olmstead, M. M.; Balch, A. L. Beyond the Butterfly:  $Sc_2C_2@C_{2v}(9)-C_{86}$ , an Endohedral Fullerene Containing a Planar, Twisted  $Sc_2C_2$  Unit with Remarkable Crystalline Order in an Unprecedented Carbon Cage. *J. Am. Chem. Soc.* **2015**, *137*, 10116–10119.
- (20) Cai, W.; Chen, C.-H.; Chen, N.; Echegoyen, L. Fullerenes as Nanocontainers That Stabilize Unique Actinide Species Inside: Structures, Formation, and Reactivity. *Acc. Chem. Res.* **2019**, *52*, 1824–1833.

- (21) Cai, W.; Abella, L.; Zhuang, J.; Zhang, X.; Feng, L.; Wang, Y.; Morales-Martínez, R.; Esper, R.; Boero, M.; Metta-Magaña, A.; Rodríguez-Fortea, A.; Poblet, J. M.; Echegoyen, L.; Chen, N. Synthesis and Characterization of Non-Isolated-Pentagon-Rule Actinide Endohedral Metallofullerenes U@C<sub>1</sub>(17418)-C<sub>76</sub>, U@C<sub>1</sub>(28324)-C<sub>80</sub>, and Th@C<sub>1</sub>(28324)-C<sub>80</sub>: Low-Symmetry Cage Selection Directed by a Tetravalent Ion. *J. Am. Chem. Soc.* **2018**, 140, 18039–18050.
- (22) Krätschmer, W.; Lamb, L. D.; Fostiropoulos, K.; Huffman, D. R. Solid  $C_{60}$ : a new form of carbon. *Nature* **1990**, 347, 354–358.
- (23) Wang, Y.; Morales-Martínez, R.; Cai, W.; Zhuang, J.; Yang, W.; Echegoyen, L.; Poblet, J. M.; Rodríguez-Fortea, A.; Chen, N. Th@ $C_1(11)$ - $C_{86}$ : an actinide encapsulated in an unexpected  $C_{86}$  fullerene cage. *Chem. Commun.* **2019**, *55*, 9271–9274.
- (24) Yang, H.; Yu, M.; Jin, H.; Liu, Z.; Yao, M.; Liu, B.; Olmstead, M. M.; Balch, A. L. Isolation of Three Isomers of  $Sm@C_{84}$  and X-ray Crystallographic Characterization of  $Sm@D_{3d}(19)$ -C<sub>84</sub> and  $Sm@C_2(13)$ -C<sub>84</sub>. J. Am. Chem. Soc. **2012**, 134, 5331–5338.
- (25) Bao, L.; Li, Y.; Yu, P.; Shen, W.; Jin, P.; Lu, X. Preferential Formation of Mono-Metallofullerenes Governed by the Encapsulation Energy of the Metal Elements: A Case Study on Eu@C<sub>2n</sub> (2n = 74–84) Revealing a General Rule. *Angew. Chem., Int. Ed.* **2020**, 59, 5259–5262.
- (26) Zhang, W.; Suzuki, M.; Xie, Y. P.; Bao, L. P.; Cai, W. T.; Slanina, Z.; Nagase, S.; Xu, M.; Akasaka, T.; Lu, X. Molecular Structure and Chemical Property of a Divalent Metallofullerene Yb@ $C_2(13)$ - $C_{84}$ . J. Am. Chem. Soc. **2013**, 135, 12730–12735.
- (27) Shen, W.; Bao, L.; Hu, S.; Yang, L.; Jin, P.; Xie, Y.; Akasaka, T.; Lu, X. Crystallographic characterization of  $Lu_2C_{2n}$  (2n = 76–90): cluster selection by cage size. *Chem. Sci.* **2019**, *10*, 829–836.
- (28) Shen, W.; Bao, L.; Wu, Y.; Pan, C.; Zhao, S.; Fang, H.; Xie, Y.; Jin, P.; Peng, P.; Li, F.-F.; Lu, X. Lu<sub>2</sub>@C<sub>2n</sub> (2n = 82, 84, 86): Crystallographic Evidence of Direct Lu-Lu Bonding between Two Divalent Lutetium Ions Inside Fullerene Cages. *J. Am. Chem. Soc.* 2017, 139, 9979–9984.
- (29) Kurihara, H.; Lu, X.; Iiduka, Y.; Nikawa, H.; Hachiya, M.; Mizorogi, N.; Slanina, Z.; Tsuchiya, T.; Nagase, S.; Akasaka, T. X-ray structures of  $Sc_2C_2@C_{2n}$  (n = 40–42): in-depth understanding of the core-shell interplay in carbide cluster metallofullerenes. *Inorg. Chem.* **2012**, *51*, 746–750.
- (30) Chaur, M. N.; Aparicio-Angles, X.; Mercado, B. Q.; Elliott, B.; Rodriguez-Fortea, A.; Clotet, A.; Olmstead, M. M.; Balch, A. L.; Poblet, J. M.; Echegoyen, L. Structural and Electrochemical Property Correlations of Metallic Nitride Endohedral Metallofullerenes. *J. Phys. Chem. C* 2010, 114, 13003–13009.
- (31) Zuo, T. M.; Beavers, C. M.; Duchamp, J. C.; Campbell, A.; Dorn, H. C.; Olmstead, M. M.; Balch, A. L. Isolation and structural characterization of a family of endohedral fullerenes including the large, chiral cage fullerenes  $Tb_3N@C_{88}$  and  $Tb_3N@C_{86}$  as well as the Ih and  $D_{5h}$  isomers of  $Tb_3N@C_{80}$ . J. Am. Chem. Soc. 2007, 129, 2035–2043.
- (32) Shen, W.-Q.; Bao, L.-P.; Hu, S.-F.; Gao, X.-J.; Xie, Y.-P.; Gao, X.-F.; Huang, W.-H.; Lu, X. Isolation and Crystallographic Characterization of  $\text{Lu}_3\text{N}@\text{C}_{2n}$  (2n = 80–88): Cage Selection by Cluster Size. *Chem. Eur. J.* **2018**, 24, 16692–16698.
- (33) Cai, W.; Morales-Martinez, R.; Zhang, X.; Najera, D.; Romero, E. L.; Metta-Magana, A.; Rodriguez-Fortea, A.; Fortier, S.; Chen, N.; Poblet, J. M.; Echegoyen, L. Single crystal structures and theoretical calculations of uranium endohedral metallofullerenes (U@C2n, 2n = 74, 82) show cage isomer dependent oxidation states for U. *Chem. Sci.* 2017, 8, 5282–5290.
- (34) Yang, H.; Jin, H. X.; Zhen, H. Y.; Wang, Z. M.; Liu, Z. Y.; Beavers, C. M.; Mercado, B. Q.; Olmstead, M. M.; Balch, A. L. Isolation and Crystallographic Identification of Four Isomers of Sm@ C<sub>90</sub>. J. Am. Chem. Soc. **2011**, 133, 6299–6306.
- (35) Saha, B.; Irle, S.; Morokuma, K. Hot Giant Fullerenes Eject and Capture C<sub>2</sub> Molecules: QM/MD Simulations with Constant Density. *J. Phys. Chem. C* **2011**, *115*, 22707–22716.

(36) Sheldrick, G. M. Acta Crystallogr., Sect. A: Found. Crystallogr. 2008, A64, 112–122.